3D hierarchical architectures based on self-rolled-up silicon nitride membranes



2013 Nanotechnology 24 475301

(http://iopscience.iop.org/0957-4484/24/47/475301)

Nanotechnology **24** (2013) 475301 (9pp) doi:10.1088/0957-4484/24/47/475301

# 3D hierarchical architectures based on self-rolled-up silicon nitride membranes

**Paul Froeter[1], Xin Yu[1], Wen Huang[1], Frank Du[2], Moyang Li[1], Iksu Chun[1], Seung Hyun Kim[1], Kuen J Hsia[3], John A Rogers[2] and Xiuling Li[1]**

[1] Department of Electrical and Computer Engineering, University of Illinois, Urbana, IL 61822, USA
[2] Department of Materials Science and Engineering, University of Illinois, Urbana, IL 61822, USA
[3] Department of Mechanical Science and Engineering, University of Illinois, Urbana, IL 61822, USA

E-mail: xiuling@illinois.edu

Received 14 August 2013, in final form 23 September 2013
Published 31 October 2013
Online at stacks.iop.org/Nano/24/475301

**Abstract**
This study presents the superior structural versatility of strained silicon nitride ($SiN_x$) membranes as a platform for three-dimensional (3D) hierarchical tubular architectures. The effects of compressive and tensile stressed $SiN_x$ layer thickness on the self-rolled-up tube curvature, the sacrificial layer etching anisotropy on rolling direction and chirality, and stress engineering by localized thickness control or thermal treatment, are explored systematically. Using strained $SiN_x$ membranes as an electrically insulating and optically transparent mechanical support, compact 3D hierarchical architectures involving carbon nanotube arrays and passive electronic components are demonstrated by releasing the functional structures deposited and patterned in 2D. These examples highlight the uniqueness of this platform that exploits 2D processing and self-assembly to achieve highly functional 3D structures.

S Online supplementary data available from stacks.iop.org/Nano/24/475301/mmedia

(Some figures may appear in colour only in the online journal)

## 1. Introduction

Strain-induced self-rolled-up membranes have attracted great interest since their emergence in 2000, fueled by their potential applications in optics, electronics, and biology [1–16]. Self-rolled-up tubes were first fabricated by Prinz *et al* by releasing a strained InAs/GaAs bilayer from a GaAs substrate using an AlAs sacrificial layer [13], wherein rolling is driven by a momentum generated between the oppositely strained InAs and GaAs layers. Since then, self-rolled-up tubes that are made of many different types of materials and precisely controlled 3D tubular architectures have been demonstrated through deposition by metalorganic chemical vapor deposition (MOCVD), molecular beam epitaxy (MBE), plasma enhanced chemical vapor deposition (PECVD), etc. Examples include epitaxial single-crystal films (e.g. InGaAs/GaAs [1, 11, 13, 17, 18], InGaAsP/InGaAsP [9], Si–Ge/Si [12]), amorphous films (e.g. $SiN_x$/Cr [19] and $SiO_x$ [4, 6, 15]), strained polymer bilayers [5], and hybrid material systems [2, 10, 16, 19–21]. Various sacrificial layers have been successfully used for the formation of tubular structures, constrained only by the etching selectivity of the sacrificial layer to the strained thin film during the final release process. These include epitaxially deposited lattice-matched heterojunctions (e.g. AlGaAs for III-As system [1, 11, 13, 17, 18] and InGaAs for III-P system [9]), evaporated thin films (e.g. Ge/$GeO_x$ [14, 22]), spun-on layers (e.g. photoresist [4, 6]), or simply commercial semiconductor substrates (e.g. Si [8, 12, 20]). Depending solely on the material system and desired tube dimensions, these films can be patterned into fully functional devices using conventional lithography before releasing and exhibit improved performance due to 3D physical, electronic, or electromagnetic confinement after releasing [1, 6, 7, 14, 23]. A clear advantage of self-rolled-up systems over other 3D patterned structures is the ability to fully functionalize the inner surface before rolling, allowing complex 3D devices to be fabricated with the precision of conventional lithography.

 

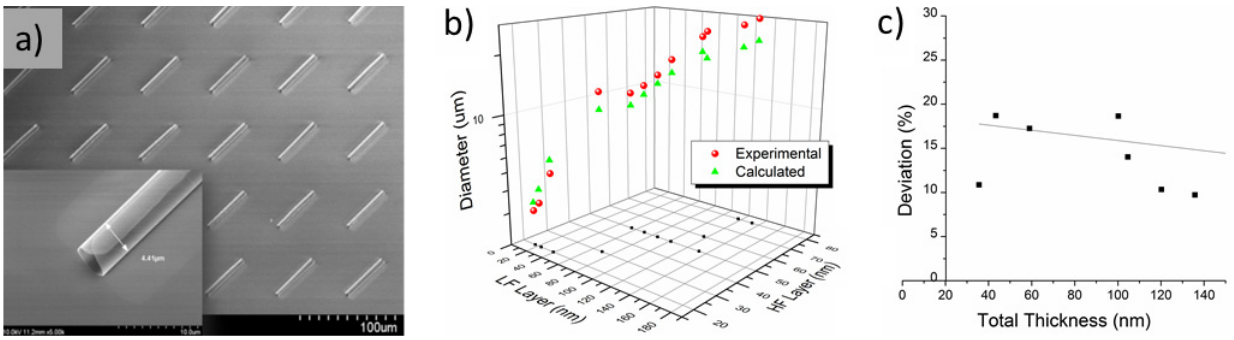


**Figure 1.** (a) Aligned array of 4.4 $\mu$m diameter tubes rolled from 39 nm LF and 20 nm HF $SiN_x$ bilayers. Inset shows a single tube at high magnification. (b) 3D plot of tube diameter as a function of the compressive (LF) and tensile (HF) $SiN_x$ membrane thicknesses (experimental: red spheres, calculated: green triangles). The planar projection of the plot (black squares) indicates the thickness combinations used for the diameter study. (c) Corresponding 2D plot of the calculated diameter deviation from the experimental value as a function of the total $SiN_x$ membrane thickness.

This work focuses on silicon nitride ($SiN_x$) based self-rolled-up microtubes, which are attractive for photonic, electronic, and biological applications, because they are transparent under visible light, tunable in refractive index, non-toxic to biological systems, inexpensive to fabricate, and compatible with Si integrated circuits. Mei *et al* demonstrated $SiN_x$ microtubes from a single-layer membrane deposited in a silane ($SiH_4$)/nitrogen ($N_2$)/helium (He) PECVD environment at high frequency (13.56 MHz) and high power (99 W) [6]. A strain gradient was created in the thin $SiN_x$ film, when deposited on photoresist (PR) at 85 °C, which resulted in tubular structures upon PR removal. In this situation the microtube diameter can be predicted by the thermal expansion coefficient mismatch between the PR and $SiN_x$. By combining the compressive strain of thermally grown silicon dioxide and the tensile strain of PECVD silicon nitride, Seleznev *et al* fabricated an integrated-circuit-ready gas sensor using hybrid $SiO_2$/$SiN_x$/Ti/Au tubular microheaters and microsensors [8]. The $SiN_x$ film was deposited in their case under high frequency in an ammonia ($NH_3$)/silane ($SiH_4$) mixture, and microtubes were formed after etching the Si substrate using ammonium hydroxide.

Unlike $SiN_x$ films deposited under high frequency (HF) at 13.56 MHz, films deposited under low frequency (LF) at 380 kHz are naturally compressively strained. Thus, oppositely strained bilayer (LF/HF) deposition can be achieved using a single tool. Unique to $SiN_x$ deposited through PECVD using ammonia/silane mixtures [24], the gas ratio of $NH_3/SiH_4$ can be adjusted to obtain a high amount of amine fragments in the film, which can result in large amounts of compressive strain and yield smaller diameter microtubes. Additionally, it provides an opportunity to augment the thin film properties after deposition. Specifically, rapid thermal annealing (RTA) allows control over film thickness, composition, and strain through ammonia outdiffusion after microtube formation.

In this paper, we report a systematic study of the fabrication of a myriad of rolled-up 3D $SiN_x$ based architectures by utilizing the tunability of $SiN_x$ film stress via PECVD deposition parameters under high and low frequency in an ammonia ($NH_3$)/silane ($SiH_4$)/nitrogen ($N_2$) system. We explore the effect of various sacrificial layers on the self-rolling behavior to realize 360° control of rolling direction and chirality, despite the isotropic strain in the $SiN_x$ bilayer. We thereafter demonstrate that $SiN_x$ microtubes can be used as a 3D mechanical support for coaxial metallic structures, carbon nanotube arrays, and other functional components.

## 2. Results and discussion

### *2.1. Control of $SiN_x$ tube diameter*

Similar to single-crystal strained films (e.g. InGaAs/GaAs), $SiN_x$ tubes of different diameters can be fabricated by varying the thickness or strain of the compressive and tensile components [17]. Figure 1(a) shows an ordered array of rolled-up $SiN_x$ microtubes with an outer diameter of 4.4 $\mu$m, formed spontaneously by releasing a 39 nm thick LF (compressive)/20 nm thick HF (tensile) $SiN_x$ bilayer deposited on a Si(111) substrate.

Figure 1(b) summarizes the experimentally measured microtube diameters as a function of LF and HF thicknesses in a 3D plot, with projection (black squares) indicating the thickness combinations used in the diameter study. As expected, the microtube diameter increases with the total thickness of the film, however it can be seen that the contribution from the LF (compressive) and HF (tensile) film thicknesses are not equal. Specifically, a disproportional diameter increase can be seen between the combinations (nm LF/nm HF) 117/60 and 117/80, respectively exhibiting diameters of 25.4 $\mu$m and 25.5 $\mu$m, compared to 117/80 and 133/80, showing an increase from 25.5 $\mu$m to 28 $\mu$m. Adapting the classical stress model for bimetallic thermostat deflection [25], the strain-induced self-rolled-up $SiN_x$ bilayer tube diameter $D$, in nm, can be expressed as:

$$D = \frac{E_1^2 t_1^4 + E_2^2 t_2^4 + 4E_1E_2(t_1^3 t_2 + t_1 t_2^3) + 6E_1E_2(t_1 t_2)^2}{3|\Delta\varepsilon|(1+\nu)E_1E_2(t_1+t_2)(t_1 t_2)} \quad (1)$$

where subscripts 1 and 2 represent LF and HF layers, respectively, $\Delta\varepsilon$ is the strain difference between LF and HF

layers, $t$ is thickness in nanometers of the individual layers ($t$), and $\nu$ is Poisson's ratio.

For the samples reported in figure 1, the residual stress, $\sigma$, in the films was measured using a FSM 500TC metrology tool to be −1168 and 406.95 MPa for the compressive and tensile strained $SiN_x$ films, respectively. The Young's modulus, $E$, of the $SiN_x$ films is proportional to the film density, which is sensitive to the deposition plasma frequency and power [26, 27]. The LF compressive film exhibits a higher Young's modulus than its HF counterpart, reported to be around 180 GPa and 170 GPa, respectively [27]. $\Delta\varepsilon$ is calculated by $\sigma_{(LF)}/E_{(LF)} - \sigma_{(HF)}/E_{(HF)}$. The diameters, using $\nu$ of 0.25 [28], are then calculated using equation (1) above. Good agreement has been found between the experimental and calculated diameters, as shown in figures 1(b) and (c). The stronger dependence of tube diameter on the compressive (LF) film thickness relative to the tensile (HF) film thickness is a result of the relatively larger Young's modulus. An overall trend of decreasing deviation with increasing total thickness between the calculated and experimental values can be seen from the linear fit shown in figure 1(c). However, a more detailed investigation will be necessary to understand and correct the deviation over a wide thickness range including much thinner films, comprising the accurate measurement of Young's modulus, additional surface stress correction [29], and the effect of substrate or sacrificial layer surface roughness.

### 2.2. 360° control of rolling direction and chirality

$SiN_x$ films deposited by PECVD differ fundamentally from epitaxial films, in that internal strain is developed not by crystal lattice mismatch, but by density differences and thermal mismatch during deposition, which can be tuned by deposition conditions. In the case of cubic single crystals such as Si or GaAs, the Young's modulus along ⟨110⟩ is larger than that along ⟨100⟩; therefore, self-rolling occurs spontaneously along the softer ⟨100⟩ direction [17, 18]. In contrast, for amorphous films including $SiN_x$, the mechanical properties are isotropic in the thin film plane; thus their rolling direction is determined by the sacrificial layer's etching behavior, isotropic or anisotropic.

$SiN_x$ microtubes arrays can readily be rolled-up along the long (a) and short (b) edges of a radially distributed rectangular pad array (figure 2). The sacrificial layer in this case is 80 nm thick polycrystalline Ge film deposited by electron beam evaporation, which can be readily etched isotropically using $H_2O_2/H_2O$ at elevated temperatures (∼80–120 °C). The microtube arrays in figures 2(a) and (b) are fabricated from the same 16 nm LF/20 nm HF bilayer patterned into identical rectangular pads, but with etching windows opened in orthogonal directions. Clearly, the rolling direction is determined by the membrane release direction, demonstrating the controllability of rolling amorphous membranes using isotropic sacrificial layers such as polycrystalline Ge. This is in clear contrast to releasing strained single-crystal InGaAs/GaAs membranes, where the rectangular pads in the radial pattern rolled-up from the ⟨100⟩ direction irrespective of the orientation of the etching window, due to the anisotropic mechanical properties of the cubic crystal thin film [18].

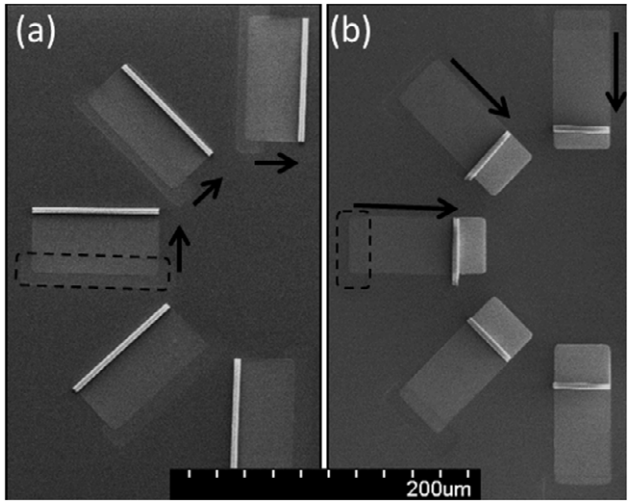


**Figure 2.** Control of rolling direction: SEM images of microtubes rolled-up rectangular-shaped $SiN_x$ thin film membranes (16 nm LF/20 nm HF) oriented in a radially distributed pattern (only half the wheels are shown). The etching window (outlined by dashed lines) is opened by optical lithography and dry etched to expose the sacrificial layer sidewall along either the long edge (a) or short edge (b) of each rectangular pad. The arrows indicate the pads' rolling directions, which originates from the etch window and proceeds forward.

It is worth mentioning that substrate surfaces with irregular morphology (such as indentations or protrusion) do not seem to prohibit the formation of microtubes when $SiN_x$ films are deposited conformally, but rather result in imprinted surface abnormalities complementary to the sacrificial layer's surface topography. Examples are provided in figure S1 of the supplemental information (available at stacks.iop.org/Nano/24/475301/mmedia).

On the other hand, using single-crystal silicon substrates allows us to exploit the etch selectivity of crystal planes through KOH or $NH_4OH$ etches, forcing $SiN_x$ films to roll preferentially in the ⟨110⟩ direction irrespective of the patterned membrane orientation. We have observed, as shown in figure S2 of the supplemental information (available at stacks.iop.org/Nano/24/475301/mmedia), that arrays of rectangular-shaped $SiN_x$ bilayers deposited on Si(111) substrates maintain near-perfect spatial order when fully released and rolled into microtubes, whereas those fabricated on Si(100) substrates are more disordered and randomly dispersed on the substrate. This is because KOH etching of Si(111) proceeds along the lateral direction (the fast etching (110) plane) preferentially, while hardly any etching takes place in the surface normal direction (the slow etching (111) plane). For (100) substrates, vertical (⟨100⟩) and lateral (⟨110⟩) etching proceed at nearly equal rates, resulting $SiN_x$ microtubes suspended far above the substrate which lose alignment when fully released.

Chiral structures can also be achieved via anisotropic etching of single-crystal sacrificial layer/substrates. We have

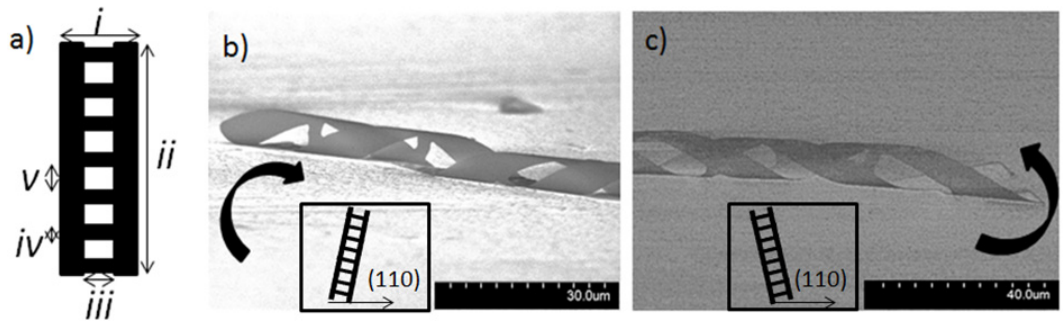


**Figure 3.** Scheme (a) of the ladder-shaped $SiN_x$ membrane geometry where all parameters *i*–*v* are defined as labeled; and tilted SEM images of rolled-up helices having left-handed (b) and right-handed (c) chirality. Dimensions *i*–*v* are 20, 204, 6, 3, and 20 $\mu$m for (b) and (c), with rotation angles of $-15°$ and $+15°$ from the (110) plane, respectively.

observed that ladder-shaped $SiN_x$ membranes with high aspect ratios can be guided into helical structures with the desired chirality within a range of misalignment angles. Specifically, by orienting a high aspect ratio rectangular pad 10°–15° off the (110) plane on a Si(111) substrate, chirality with a predictable rotation angle and turn-to-turn pitch can be obtained.

Figure 3(a) shows the design of ladder-shaped rectangular strips of a $SiN_x$ membrane with a total width of *i* and length of *ii*. The ladder rung dimensions are given by a width of *iii*, height of *iv*, and spacing between ladder steps of *v*. As in the case of microtubes, the curvature of the rolled-up helical structures are determined by the embedded strain, but the amount of overlap or spacing from turn-to-turn (pitch) and chirality are determined by the ladder geometry and degree of rotation off of the fastest etch plane. This architecture simulates the DNA-like double helix structure, where ladder rungs are analogous to DNA base pairs. Shown in figures 3(b) and (c) are two rolled-up membranes demonstrating a double helix with complementary rotations (left-hand for 3(b) and right-hand for 3(c)). This has been achieved by orienting the strips ($i = 20$ $\mu$m, $ii = 204$ $\mu$m, $iii = 6$ $\mu$m, $iv = 3$ $\mu$m, and $v = 20$ $\mu$m) by 15° relative to (110) facets to the left or right, as illustrated in the figure insets. To explore the geometry effects of chirality controllability, ladder structures were patterned with varying pad aspect ratios and 'base pair' dimensions over a parameter space detailed in table S3 in the supplemental information (available at stacks.iop.org/Nano/24/475301/mmedia), while film thickness was held constant at 55 nm LF/20 nm HF. We found that all pads oriented at an angle 15° clockwise, relative to (110) facets, (figure 3(b)) experienced etching first on the bottom left and top right corners, resulting in left-hand chiral double helixes, and vice versa for counterclockwise rotation (figure 3(c)). High uniformity of the chiral structure formation was found in ladders with offset angles of 15°, high aspect ratios ($ii/i \geq 10$ $\mu$m), and large rung spacings ($v \geq 15$ $\mu$m). Note that long pads suffer from the isotropic nature of the strained $SiN_x$ bilayer, expanding in both dimensions and creating periodic wrinkling prior to release.

As expected, ladders oriented perpendicular to the (110) plane experienced nearly symmetric etching and, with the exception of the highest aspect ratio pad, rolled into tubes exhibiting no chirality. In this case the areas near the rungs are the slowest etching ones, and thus the last points of contact before full release of the thin film resulting in symmetric rolling. Chiral uniformity among different aspect ratio ladders decreases when the offset angle deviates from 15°. Beyond a ±3° tolerance, the aspect ratio becomes the dominant chirality control factor. Owing primarily to a greater torque before full release, high aspect ratio (long and narrow) ladders are more likely to form a double helix, whereas shorter, wider pads more often exhibited no chirality. In SiGe/Si/Cr trilayers reported previously, the chirality direction was predicted based on sacrificial layer asymmetry for pad widths up to 1 $\mu$m [20, 30]. In comparison, the ladder structures explored here have total pad widths greater than 1 $\mu$m, periodic spacing between ladder rungs, and are made of an amorphous thin film. Longer pads with larger rung spacings ($v \geq 15$ $\mu$m) are most consistent with predictions [20] for obtaining helices from a single high aspect ratio rectangular pad, due to the high aspect ratio between ladder rungs. Short, wide ladders suffer from buckling ladder rungs, inducing an additional strain vector and reducing the overall torque. Because of this, random rolling behavior was observed in ladders having a low aspect ratio ($ii/i \leq 8$ $\mu$m) and long rungs ($iii \geq 7$ $\mu$m) with narrow spacing ($v \leq 6$ $\mu$m) over all offset angles. Additionally, at offset angles less than 10°, low aspect ratio ladders exhibited no chirality, while higher aspect ratio ladders at the same offset angle rolled normally. The formation of DNA-like helical structures, enabled by the amorphous $SiN_x$ membranes through anisotropic release, could lead to unique Janus architectures if functional structures or materials can be patterned in 2D before release. The effect of aspect ratio, offset angles, and ladder rung spacing on chirality reported here provides basic boundary conditions for fabricating such chiral structures. Future studies will include systematic modeling to establish the relationship between mechanical torque due to ladder rung spacing and chirality as a function of geometry.

### *2.3. Structural hierarchy by local stress control*

Local curvature modulation in the rolled-up structures due to thickness or stress variation can also be used to create unique

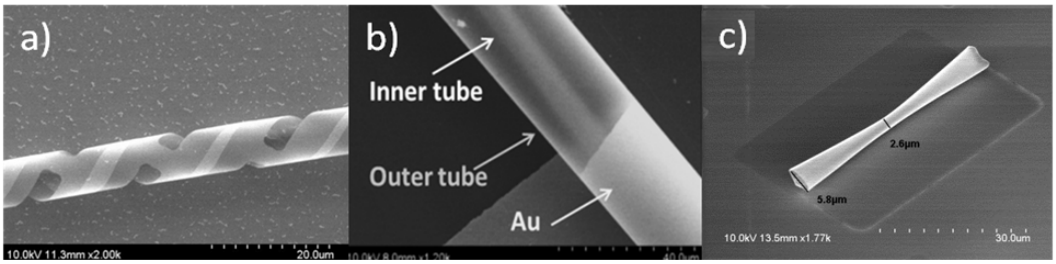


**Figure 4.** (a) Local thickness variations in chiral tubes induced by angular alignment variations relative to the (110) etch plane on a Si(111) substrate. (b) Coaxial tube arrays due to addition of compressively strained Au (70 nm) onto a 16 nm LF/20 nm HF $SiN_x$ bilayer. (c) Local diameter variations (5.8–2.6 $\mu$m) in 50 $\mu$m long single-roll microtubes subjected to a post-rolling anneal at 600 °C for 60 s.

3D hierarchical architectures. This can be achieved through either pre-rolling fabrication steps or a post-rolling thermal processing. Thickness variation can be created in high aspect ratio pads by forcing a membrane to overlap itself as it is released from the substrate. As seen in figure 4(a), a high aspect ratio ladder ($i = 17$ $\mu$m, $ii = 451$ $\mu$m, $iii = 5$ $\mu$m, $iv = 3$ $\mu$m, and $v = 25$ $\mu$m) is patterned onto a 39 nm LF/20 nm HF $SiN_x$ bilayer and offset at 10° to the left, relative to the (110) facet, to achieve an overlapping chiral structure, improving rigidity. In addition, the turn-to-turn overlap distance can be modulated within the same microtube (overlap is seen as bright areas in SEM). This can be useful in achieving large bandwidth RF components, as each overlapping area has a different capacitance and inductance [14]. Strain gradients resulting from additional thin films can also be used as a pre-rolling curvature modulation technique. Materials with different internal stress or thickness will result in a diameter change and can be used, as seen in figure 4(b), to achieve coaxial and triaxial architectures.

By patterning a second level stress material (e.g. Au) in selected areas on strained $SiN_x$ membranes, the curvature of the rolled-up $SiN_x$ structures can be changed locally. Figure 4(b) shows a coaxial tube structure, where the inner tube (smaller diameter) consists of a 39 nm LF/20 nm HF $SiN_x$ film and the outer tube (larger diameter) consists of an additional 70 nm thick Au film on the lower end (bright opaque area) while the upper end is the same $SiN_x$ film as the inner tube (transparent). This was achieved by carefully placing the Au layer right after the $SiN_x$ membrane finishes its first turn with a diameter of ~7 $\mu$m. When the second turn encounters the Au + $SiN_x$ film (with a total thickness of 129 nm), the reduced torque causes the diameter to increase to ~28 $\mu$m, creating a gap between the first and second turn. Similarly, a third level stress layer can be patterned at locations after the second turn to induce a gap between the second and third turn; and so on so forth. These gaps can be engineered by simply changing the thicknesses of the additional layers, allowing coaxial and triaxial microtubes on the same substrate. Note that the additional layer (Au in this case) can be continuous or discrete. In the latter case, the width and spacing of the Au pads are important when designing coaxial microtubes. If the Au pads are separated too far apart, the microtube can tear or collapse instead of assuming the same diameter as areas with the Au pads, owing to the difference between relaxed diameters. Detailed design, simulation, and fabrication of local stress control using patterned conductive strips for passive electronic components will be reported separately.

In addition, curvature variations can be engineered through post-rolling thermal processing when $SiN_x$ film is deposited using a $SiH_4$ and $NH_3$ mixture. The detailed chemistry of the $SiN_x$ formation process can be found in section 4. The $SiN_x$ microtube diameter can be reduced when subjected to thermal annealing at a temperature above the deposition temperature (300 °C), as a result of $NH_3$ outdiffusion. Shown in figure 4(c), a 60 s anneal at 600 °C in $N_2$ atmosphere results in as much as a 2× reduction in diameter at the center of the microtube relative to the ends, resulting in a graduated cone architecture. The as-rolled-up tube diameter and length were 4.2 and 50 $\mu$m, respectively. We believe the uneven reduction in diameter along the tube is a result of a local thermal gradient along the microtube axis, where heat is trapped in the center and more dissipation occurs at the ends. Depending on the length of the tube and local thermal engineering, various unique structures can be created using this mechanism. Locally constrained microtubes can be useful as low-pass filters in microfluidic channels, where the channel radius has a large impact on the inertia and friction experienced by the fluid.

### *2.4. 3D hierarchical architectures by heterogeneous integration*

By using $SiN_x$ strained bilayers as a vehicle to roll-up other materials, multi-turn tubular architectures consisting of metals, semiconductors, dielectrics, or polymers can be produced. Depending on the amount of additional stress introduced upon the bilayer, the rolled-up hybrid tube can have a larger or smaller diameter than the bilayer itself. Chrome (Cr) and nickel (Ni), with well characterized strain at nearly every deposition rate and thickness [31], can be used to provide greater tensile stress than the HF $SiN_x$ layer. For example, a 9% diameter reduction is seen from a hybrid microtube consisting of 16 nm LF $SiN_x$/20 nm HF $SiN_x$/5 nm Cr compared to the 16 nm LF/20 nm HF $SiN_x$ bilayer alone. Cr can also be deposited such that it replaces the HF $SiN_x$ layer to provide the tensile strain.

Shown in figure 5(a) is a rolled-up metal-$SiN_x$ hybrid structure that consists of a stack metal layer (5 nm Ni/60 nm Au/5 nm Ni) patterned into parallel square turning meander

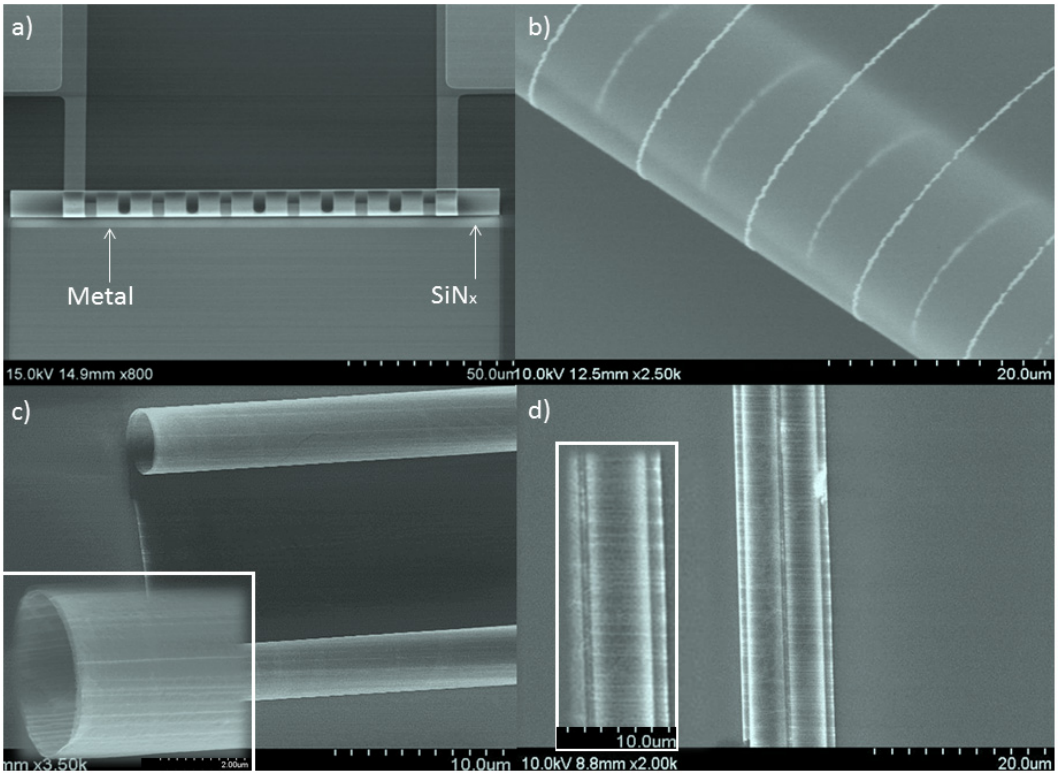


**Figure 5.** SEM images of silicon nitride based hierarchical hybrid tubes. (a) An inductor design consisting of four turns of 5 nm Ni/60 nm Au/5 nm Ni square wave pattern, rolled-up by a 36 nm strained $SiN_x$ bilayer. (b) 16 nm LF $SiN_x$/20 nm HF $SiN_x$/7 nm Cr (exposed)/70 nm Au quadlayer rolled downward due to local stress from chromium oxide, (c) carbon nanotube (CNT) arrays aligned along the axial direction within a rolled-up $SiN_x$ microtube (inset: zoomed-in image of the microtube end, showing CNTs as high contrast lines), and (d) CNT arrays aligned along the radial direction within a rolled-up $SiN_x$ microtube (inset: zoomed-in image of the microtube midsection, showing the gap between microtube rotations).

strips on a strained $SiN_x$ bilayer, yielding a radial superlattice of $(SiN_x/\text{metal})_n$. The rolling direction is from the bottom up, as indicated by the arrows. The number of windings in this case is four and the inner diameter is 8 $\mu$m. This structure can function as a compact inductor with the strained $SiN_x$ film not only serving as the vehicle to reduce the footprint, but also as the insulation between turns of metal. The metal strip in each winding (radial direction) carries current flowing in the same direction, thus more windings are required to achieve higher inductance. More metal strips along the tube axis will also lead to higher inductance, but since adjacent strips carry opposite current they have to be spaced far apart in order to minimize canceling inductance. The detailed theory of the rolled-up inductor design, targeting miniaturization and performance enhancement, can be found in [14] and electrical performance will be reported separately. Any conductive thin film can be patterned and rolled-up in similar fashion to form metallic windings, provided the material resists the sacrificial layer etchant and there is sufficient net strain embedded in the hybrid thin film. The rolling direction can even be dynamically changed if the net strain direction reverses during the rolling process. Shown in figure 5(b) is a scroll of parallel thin (broken) Au lines rolled downward instead of up. This was realized by subjecting a quadlayer, consisting of 16 nm thick LF $SiN_x$, 20 nm thick HF $SiN_x$, 7 nm thick Cr thin film, and 70 nm thick and 1 $\mu$m wide Au lines, to a RCA SC1 solution (5-DI:1–30%$H_2O_2$:1–30%$NH_4OH$) at 75 °C to etch a germanium sacrificial layer. Initially, the released membrane experienced a torque that rolls the membrane upward. As etching proceeded, Cr was rapidly oxidized when encountering the SC1 solution, resulting in the formation of a compressively strained chromium oxide ($CrO_2$) layer. The torque from the oxidized chrome resulted in unrolling followed by downward rolling, yielding the image shown in figure 5(b). Note that the rapid oxidation and expansion of the underlying Cr layer has also caused partial delamination of the Au lines, resulting in broken and thinner lines as shown. Downward rolling can also be readily achieved by reversing the strain direction of the $SiN_x$ bilayer. However, patterning Cr in selected areas allows dynamic upwards rolling and downwards rolling triggered during releasing.

Figures 5(c) and (d) show rolled-up CNT structures where a 16 nm LF/20 nm HF $SiN_x$ bilayer is used as a vehicle to roll-up aligned CNT arrays, with CNTs aligned along the axial and radial directions, respectively. Aligned CNTs grown from Fe catalyst lines (5 Å thick, 10 $\mu$m wide, 100 $\mu$m pitch) were first transferred (including Fe) to the strained $SiN_x$ bilayer with an average density of 5 CNTs $\mu m^{-1}$. The $SiN_x$/CNTs hybrid membrane is then released and rolled-up from both sides of the pad when the Ge sacrificial layer is removed in $H_2O_2$. This yields a 4 $\mu$m diameter final structure having a radial superlattice of $(SiN_x/\text{CNT})_n$, where

$n$ is the number of windings, and effectively increases the density of CNTs by $n$ times. As expected, CNTs have no measurable influence on the local strain and do not change the diameter of the $SiN_x$ microtubes relative to the bilayer alone. Note that the outer edges of the microtubes in figure 5(d) appear to have gaps, which result from the decreased torque experienced in the area surrounding the now oxidized Fe catalyst strip (10 $\mu$m wide). Similar to the coaxial tube in figure 4(b), the compressively strained strip forces the microtube diameter to increase by $\sim$2 $\mu$m, so that a 1 $\mu$m gap is created between turns. However, the $SiN_x$/CNTs membrane retracts back to the original curvature after passing the Fe strip (100 $\mu$m pitch), resulting in a gap approximately every eight turns. The hierarchical structure created this way can serve as a platform for high density and small footprint CNT based devices. Additionally, this hybrid membrane can provide a mechanism to incorporate CNTs into 3D structures for mechanical reinforcement, taking advantage of the high tensile strength of CNTs and decreasing the probability of $SiN_x$ membrane shearing, discussed previously.

## 3. Conclusion

In this study, strained $SiN_x$ membranes have been demonstrated as a versatile platform to achieve unique rolled-up 3D hierarchical structures. The control of compressive and tensile strain in low frequency and high frequency plasma CVD enables monolithic control of the diameter of rolled-up tube arrays. Additional strained layers enable the control of upwards and downwards rolling, as well as the dynamic nature of certain material combinations. The amorphous nature of the film allows 360° control of the rolling direction by lithographical patterning. Combined with the sacrificial layer etching orientation dependence, helical structures with defined chirality are realized. Local stress control allows the creation of hierarchical structures, including coaxial tubes with controlled gap between turns or a lateral gradient of curvature. Rolling-up functional materials, including metal lines and CNTs arrays, using strained $SiN_x$ membranes as a vehicle, presents a pathway to create complex 3D architectures that can potentially lead to advanced functionalities that are otherwise out of reach. Essentially, the processing method demonstrated in this study, in which 3D architectures are fabricated simply by releasing strained 2D hybrid membranes, represents a new design and fabrication paradigm that processes like 2D and functions like 3D.

## 4. Methods

### *4.1. Growth and characterization of silicon nitride thin films*

A STS mixed frequency nitride PECVD system was used for the deposition of $SiN_x$ thin films. Depending on deposition parameters such as pressure, gas flow ratio and rate, substrate temperature, and RF power and frequency, $SiN_x$ films deposited using a $NH_3/SiH_4/N_2$ gas mixture can show a range of densities from 2 to 2.5 mg $cm^{-3}$ and refractive indices from 1.8 to 2.35 [32]. Stress embedded within the film is directly related to density and refractive index, and thus can also be varied widely depending on deposition parameters. The overall reaction for $SiN_x$ films deposited using an $NH_3/SiH_4/N_2$ plasma [24] is:

$$\begin{aligned} &SiH_4(g) + 4NH_3(g) \overset{\text{Plasma}}{\rightarrow} Si(NH_2)_4(s) + 4H_2(g) \\ &\qquad \text{at} \quad 80\text{–}300\,^{\circ}\text{C} \\ &3Si(NH_2)_4(s) \overset{\text{Anneal}}{\rightarrow} Si_3N_4(s) + 8NH_3(g) \\ &\qquad \text{at} \quad T \geq \text{deposition } T. \end{aligned} \tag{2}$$

Compared to other CVD processes, using a $NH_3/SiH_4/N_2$ PECVD allows lower processing temperatures and creates an amine-rich membrane. Because of this, the film thickness, geometry, and diameter can be drastically altered after rolling via a high temperature RTA, due to outdiffusion of embedded hydrogen and ammonia within the $SiN_x$ film, as shown in equation (2). (See figure 3(c) and related discussions.)

Both tensile and compressive, as well as zero (compensated), stress can be produced in the film, depending primarily on the operating plasma frequency. Compressive stress is generated at high power and low frequency (LF), whereas tensile stress dominates at high frequency (HF). Low pressure promotes compressive stress by providing a longer mean-free-path for the radicals in the plasma, allowing more to reach the surface for a denser, and thus more compressively strained film [27]. In this study, compressive $SiN_x$ was deposited at 60 W, 380 kHz, 550 mTorr, and 240 °C, resulting in $-1168$ MPa of residual compressive stress, as measured using a FSM 500TC. In comparison, tensile $SiN_x$ was deposited at 20 W, 13.56 MHz, 900 mTorr, and the same temperature, resulting in $+406.95$ MPa of residual tensile stress. $SiH_4$, $NH_3$, and $N_2$ flow rates and ratios widely affect the embedded strain of the film, as reported in [32]. For this study, 40.0 sccm of $SiH_4$ and 20 sccm of $NH_3$ ($SiH_4/NH_3$ ratio of 2) was used to create the compressively strained $SiN_x$ film, in addition to the parameters previously outlined. Likewise, in addition to the higher frequency and pressure, 40.0 sccm of $SiH_4$ and 55.0 sccm of $NH_3$ (ratio of 0.72) was used to create the tensile layers used in this study. $N_2$ flow was kept constant at 1960 sccm. Further details of the deposition conditions can be found in section S3 of the supplemental information (available at stacks.iop.org/Nano/24/475301/mmedia).

### *4.2. Fabrication process of rolled-up silicon nitride microtubes*

The process flow for fabricating rolled-up $SiN_x$ microtubes is shown in figure 6.

Using process parameters previously discussed, a strained $SiN_x$ bilayer film was deposited using the low (compressive strain) and high (tensile strain) frequency conditions sequentially 6(b), on the sacrificial layer and substrate 6(a). Photolithography was then carried out to define the dimension of the membrane 6(c), followed by dry etching 6(d) through the $SiN_x$ bilayer and beyond the sacrificial layer using Freon 14 ($CF_4$) reactive ion etching (RIE). This

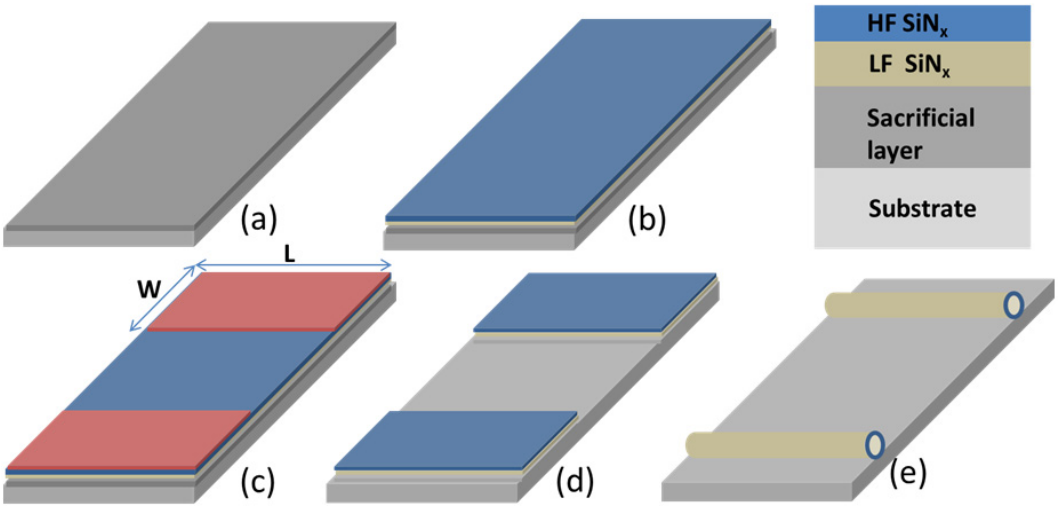


**Figure 6.** Schematic illustration of process flow of the fabrication of silicon nitride tubes. (a) Clean substrate and deposit sacrificial layer (e.g. Ge on glass), (b) deposit low frequency (LF, compressive) and high frequency (HF, tensile) strained silicon nitride film, (c) define pads lithographically using photoresist (red colored), (d) dry etch through the stack into the sacrificial layer using $CF_4$, and (e) etch the sacrificial layer to release the strained membrane to enable self-rolling. The color denotation is illustrated on the upper right.

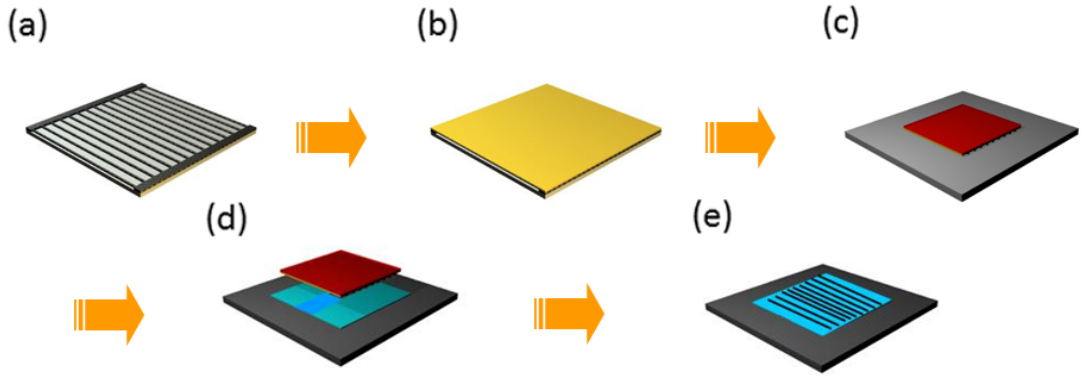


**Figure 7.** Schematic of CNT polymer transfer onto the SiN bilayer. (a) Grow aligned CNTs on quartz, (b) drop-cast polymer (gold) and anneal at 65 °C, (c) attach thermal tape (red) and cut away edges, (d) transfer CNT + PVA + tape onto the $SiN_x$ substrate (blue), remove thermal tape by heating at 90 °C, (e) and remove polymer using DI.

is to ensure exposure of the sacrificial layer sidewalls to the etchant, leading to uniform lateral etching, membrane release, and rolling 6(e). Depending on the dimension of the pad defined in step 6(c), the released $SiN_x$ membrane rolls-up spontaneously along the long side ($L$) or short side ($W$) during the sacrificial layer etch. Our dimensions remained within a $L/W$ ratio of 2.5–8 (7.7–26.5 for chirality experiments) and a $T/W$ ratio of 0.0036–0.01 (0.0034–0.01 for chirality experiments). These values were predicted from data points which satisfy geometric conditions for rolling single-crystal strained membranes from their long side or corners, respectively [33].

Various substrates including crystalline Si(100), Si(111), and glass were used for this study. Different sacrificial layers were explored to release the strained $SiN_x$ films, including crystalline silicon, amorphous a-Si, Ge, $GeO_2$, and aluminum (Al); various material combinations allowing high etch selectivity between sacrificial layer and strained $SiN_x$ film. For single-crystal Si, the crystal orientation dependent anisotropic etching effect can be readily used to release silicon nitride films directly from Si(100) and (111) substrates into ordered microtube arrays. Typically, 45% potassium hydroxide (KOH) solution heated to 47 °C is used, yielding a typical lateral etch rate of 380 nm $min^{-1}$. The MOS compatible ammonium hydroxide ($NH_4OH$) can also be used for such etching [7]. In the case of evaporated Ge sacrificial layers, a 30% $H_2O_2$ solution heated to 70 °C was used to etch at a rate of 480 nm $min^{-1}$. Alternatively, germanium oxide can be used as a sacrificial layer, either directly deposited or by oxidizing evaporated Ge, achieving a lateral etch rate of 840 nm $min^{-1}$ in room temperature DI water. Although processing with germanium oxide has more restraints, it is advantageous in situations that prohibit the use of stronger etchants.

The process of transferring the CNT array from its native growth substrate onto the silicon nitride bilayer film was developed to be compatible with the $SiN_x$ bilayer and is illustrated in figure 7. CNT hybrid microtubes were transferred over to glass slides having a Ge/LF $SiN_x$/HF $SiN_x$ stack, defined via RIE, and wet etched using $H_2O_2$, releasing the microtube. (See figure 5 and related discussions.) Details of the growth method for CNT arrays can be found

in [34]. Briefly, 0.5 nm thick Fe catalyst lines were deposited on quartz substrates and growth was done at 925 °C under 20 sccm of Ar and 20 sccm of $H_2$, bubbled through chilled ethanol, yielding aligned CNT densities of typically 5 $\mu m^{-1}$ (7(a)). SWNTs are successively encapsulated in PVA (polyvinyl alcohol) and annealed at 65 °C for 1 h. Thermal tape is placed over the hardened PVA and edges are cut away, as seen in figures 7(b) and (c). The resulting film is transferred via thermal release tape and, once transferred onto the receiving substrate, is heated by the receiving substrate (90 °C) to allow removal of the tape (7(d)). Finally, the PVA is washed away with water, leaving pristine, perfectly aligned CNTs.

## Acknowledgments

The authors gratefully acknowledge financial support provided by the US Department of Energy, Office of Basic Energy Sciences, Division of Materials Sciences and Engineering under Award No. DE-FG02-07ER46471 (PF, ML, FD, KJH, JAR, and XL), NSF ECCS Award No. 0747178 (IC, XY), and No. 1309375 (SHK, WH).

## References

[1] Li X 2008 *J. Phys. D: Appl. Phys.* **41** 193001
[2] Songmuang R, Rastelli A, Mendach S, Deneke C and Schmidt O G 2007 *Microelectron. Eng.* **84** 1427
[3] Yu M, Huang Y, Ballweg J, Shin H, Huang M, Savage D E, Lagally M G, Dent E W, Blick R H and Williams J C 2011 *ACS Nano* **5** 2447
[4] Huang G S, Kiravittaya S, Quiñones V A B, Ding F, Benyoucef M, Rastelli A, Mei Y F and Schmidt O G 2009 *Appl. Phys. Lett.* **94** 141901
[5] Luchnikov V, Kumar K and Stamm M 2008 *J. Micromech. Microeng.* **18** 035041
[6] Mei Y, Huang G, Solovev A A, Ureña E B, Mönch I, Ding F, Reindl T, Fu R K Y, Chu P K and Schmidt O G 2008 *Adv. Mater.* **20** 4085
[7] Huang G and Mei Y 2012 *Adv. Mater.* **24** 2517
[8] Seleznev V A, Prinz V Y, Aniskin V M and Maslov A A 2009 *J. Appl. Mech. Tech. Phys.* **50** 291
[9] Bianucci P, Mukherjee S, Poole P and Mi Z 2011 Self-organized 1.55 $\mu$m InAs/InP quantum dot tube nanoscale coherent light sources *Winter Topicals (WTM), 2011 IEEE* vol 4, pp 127–8
[10] Golod S V, Prinz V Y, Wägli P, Zhang L and Kirfel O 2004 *Appl. Phys. Lett.* **84** 3391
[11] Mi Z, Bianucci P, Dastjerdi M H T, Mukherjee S, Tian Z, Veerasubramanian V, Kirk A G and Plant D V 2011 1.3–1.55 $\mu$m self-organized InAs quantum dot tube nanoscale lasers on silicon *Photonics Conf. (PHO), 2011 IEEE* vol 6, pp 535–6
[12] Golod S V, Prinz V Y, Mashanov V I and Gutakovsky A K 2001 *Semicond. Sci. Technol.* **16** 181
[13] Prinz V Y, Seleznev V A, Gutakovsky A K, Chehovskiy A V, Preobrazhenskii V V, Putyato M A and Gavrilova T A 2000 *Physica* E **6** 828
[14] Huang W, Yu X, Froeter P, Xu R, Ferreira P and Li X 2012 *Nano Lett.* **12** 6283
[15] Schulze S, Huang G, Krause M, Aubyn D, Quiñones V A B, Schmidt C K, Mei Y and Schmidt O G 2010 *Adv. Eng. Mater.* **12** B558
[16] Luo J K, Huang R, He J H, Fu Y Q, Flewitt A J, Spearing S M, Fleck N A and Milne W I 2006 *Sensors Actuators* A **132** 346
[17] Chun I S, Verma V B, Elarde V C, Kim S W, Zuo J M, Coleman J J and Li X 2008 *J. Cryst. Growth* **310** 2353
[18] Chun I S and Li X 2008 *IEEE Trans. Nanotechnol.* **7** 493
[19] Arora W J, Nichol A J, Smith H I and Barbastathis G 2006 *Appl. Phys. Lett.* **88** 053108
[20] Dai L and Zhang L 2013 *Nanoscale* **5** 971
[21] Moiseeva E, Senousy Y M, McNamara S and Harnett C K 2007 *J. Micromech. Microeng.* **17** N63
[22] Bufon C C B, González J D C, Thurmer D J, Grimm D, Bauer M and Schmidt O G 2010 *Nano Lett.* **10** 2506
[23] Shiplyuk A N, Aniskin V M, Seleznev V A, Prinz V Y, Maslov A A and Matvienko R S 2009 *J. Appl. Mech. Tech. Phys.* **50** 454
[24] Smith B, Alimonda D, Chen A, Ready C and Wacker S 1990 *J. Electrochem. Soc.* **137** 614
[25] Timoshenko B Y S 1925 *J. Opt. Soc. Am.* **11** 233
[26] Mi Z 2010 *Photon. Technol. Lett.* **22** 311
[27] Li W, Kang Z, Ye Y and Jiang Y 2010 Influences of process parameters of low frequency PECVD technology on intrinsic stress of silicon nitride thin films *Proc. SPIE 7658, 5th Int. Symp. on Advanced Optical Manufacturing and Testing Technologies: Optoelectronic Materials and Devices for Detector, Imager, Display, and Energy Conversion Technology* vol 7658, p 765824
[28] Walmsley B A, Liu Y, Hu X Z, Bush M B, Dell J M, Faraone L and Member S 2007 *J. Microelectromech. Syst.* **16** 622
[29] Zang J, Huang M and Liu F 2007 *Phys. Rev. Lett.* **98** 146102
[30] Dai L and Shen W Z 2009 *J. Appl. Phys.* **106** 114314
[31] Doerner M F and Nix W D 1988 *Crit. Rev. Solid State Mater. Sci.* **14** 225
[32] Gorin A, Jaouad A, Grondin E, Aimez V and Charette P 2008 *Opt. Express* **16** 13509
[33] Chun I S, Challa A, Derickson B, Hsia K J and Li X 2010 *Nano Lett.* **10** 3927
[34] Du F and Rogers J A 2013 Aligned arrays of single walled carbon nanotubes for transparent electronics *Proc. SPIE 8725, Micro- and Nanotechnology Sensors, Systems, and Applications V* vol 8725, p 87251S